Journal of The Electrochemical Society, 2025 **172** 056510

Nb:TiO_2 Protection Layers for FTO-based Cathodes for CO_2 Reduction Under Neutral Conditions

Yu-Lin Tsai,[1,2] Karsten Harbauer,[1] Siddharth Gupta,[1,3] Matthew T. Mayer,[1] Peter Bogdanoff,[1,z] and Roel van de Krol[1,2]

[1]*Helmholtz-Zentrum Berlin für Materialien und Energie GmbH, Hahn-Meitner-Platz 1, 14109 Berlin, Germany*
[2]*Institut für Chemie, Technische Universität Berlin, Straße des 17. Juni 124, 10623 Berlin, Germany*
[3]*Institut für Chemie und Biochemie, Freie Universität Berlin, Arnimallee 20, 14195 Berlin, Germany*

With the rising anthropogenic CO_2 concentrations in the atmosphere and the growing interest in converting solar energy into value-added products, interest in (photo)electrochemical reduction of CO_2 is increasing. A key component for this process is an optically transparent and electrically conductive substrate, usually in the form of a transparent conducting oxide (TCO) film deposited on glass. However, most traditional TCO materials, such as fluorine-doped SnO_2 (FTO) or tin-doped In_2O_3 (ITO), are not stable under cathodic conditions. TiO_2 has been widely reported as an excellent protection layer material in photo-electrochemical (PEC) research, and niobium is one prospective dopant to improve its conductivity. In this work, we demonstrate that commercial FTO glass can be protected against (photo)corrosion under cathodic reaction conditions in pH-neutral electrolytes by direct-current sputtering of thin Nb-doped TiO_2 (Nb:TiO_2) overlayers. Combined with a pre-deposition FTO etching procedure, the Nb:TiO_2-covered FTO electrode offers excellent electrochemical stability while maintaining good transparency and conductivity.
 [DOI: 10.1149/1945-7111/add9d4]

Manuscript submitted January 22, 2025; revised manuscript received March 24, 2025. Published May 29, 2025.

Supplementary material for this article is available online

Among various transparent conducting oxides (TCOs), commercially available fluorine-doped tin oxide (FTO) is a widely used substrate for optoelectronics and thin film photovoltaics. It also has a pivotal role in electrochemical research owing to its availability, relatively low toxicity, good transparency, good conductivity, and chemical stability.[1,2] It is commonly employed in various fields including thin film solar cells,[3] dye-sensitized solar cells (DSSC),[4,5] photo-electrochemical (PEC) water splitting,[6,7] PEC glycerol oxidation,[8,9] PEC H_2O_2 production,[10] PEC wastewater treatment,[11] and other PEC oxidation reactions.[12,13] According to the Pourbaix diagram, it is especially suitable for photoanodes in PEC research because of its chemical stability under a wide span of anodic potentials.[14] With increasing interest in converting solar energy to value-added products using cathodic reduction reactions, the demand for a transparent, conductive, and stable substrate at cathodic potentials grows accordingly. In particular, we like to highlight photo-driven electrochemical CO_2 reduction, which is increasingly attracting interest due to the increasing anthropogenic CO_2 concentration in the atmosphere.[15–27]

Unfortunately, FTO is thermodynamically unstable under potentials more negative than roughly -0.12 V_{RHE} in a neutral electrolyte, as SnO_2 is prone to being electrochemically reduced to metallic Sn.[14] Electrochemical CO_2 reduction is usually conducted in a pH-neutral electrolyte and at overpotentials more negative than -0.3 V_{RHE}, where FTO corrosion is thermodynamically inevitable. The formed Sn particles will not only obscure the true activity of the deposited catalysts under investigation (Sn possesses its own activity towards CO_2 reduction), but also cause the substrate to lose its optical transparency.

Finding TCO substrates that are stable under electrochemically reducing conditions might be achieved by exploring completely new TCO materials, but this is likely to be fairly time and resource consuming. In contrast, protecting commercially available FTO glass against corrosion by functionalizing it with a protection layer might be an easier and more attractive approach.

TiO_2 has long been identified as a suitable protection layer material because of its wide bandgap and good chemical stability over a wide range of conditions. Lee et al. reported stable operation of p-InP nanopillar photocathodes covered with a thin TiO_2 protection layer made by atomic layer deposition (ALD) for up to 4 h, demonstrating a solar-to-hydrogen conversion efficiency of 14%.[28] Paracchino et al. demonstrated up to 10 h of stable operation for Cu_2O photocathodes protected with thin Al:ZnO (AZO) and TiO_2 overlayers deposited by ALD.[29,30] ALD-TiO_2 was also used by Seger et al. to protect n^+p Si photocathodes that showed stable PEC hydrogen evolution for up to 2 weeks with minimal degradation.[31] Cao et al. used an ALD-TiO_2 protection layer to stabilize a microdome-structured p-GaAs photocathode for up to 60 h,[32] while Cui et al. demonstrated stable PEC water splitting operation for 67 h without obvious decay using ALD-TiO_2 protected GaAs nanowires (NWs) as photoelectrode.[33] Song et al. reported the use of ALD-TiO_2 protection layer to stabilize FTO/$CuBi_2O_4$ photocathodes, demonstrating PEC hydrogen production from a $BiVO_4$–$CuBi_2O_4$-based tandem cell.[34] At this point it should be noted that TiO_2 also shows a minor activity for CO_2 reduction. It has been reported that Ti^{IV}/Ti^{III} redox centers, formed under negative applied potentials, stabilize CO intermediates and support the CO_2 reduction.[35–37] However, the catalytic activity of TiO_2 is relatively low when compared to that of metallic tin particles. Whether the enhanced charge transfer by the Ti^{IV}/Ti^{III} centers could stabilize the TiO_2 layer is not yet fully understood. Regardless, TiO_2 is reported to be chemically stable in neutral electrolytes also without the presence of CO_2.[32]

Since pure TiO_2 is not a good electronic conductor, the thickness of these ALD protection layers is typically limited to 10–20 nm. Thicker layers would offer more robust protection but require a higher electronic conductivity of the TiO_2. For this reason, dopants (for instance Zn,[38,39] Al,[40,41] Nb,[42–51] or Ta[52]) are often incorporated. Nb-doped TiO_2 (Nb:TiO_2 or NTO) is one of the promising highly conductive metal oxide materials that has been made by various deposition techniques, including direct-current magnetron sputtering,[43,44,46,50] radio-frequency magnetron sputtering,[49] atomic layer deposition,[28–33,48,51,53–55] and pulsed laser deposition (PLD).[42,43,47,56]

In this work, we report on the use of direct-current (DC) magnetron sputtering as a method to prepare thin Nb:TiO_2 protection layers on commercial FTO glass. The electrochemical stability of these glass/FTO/NTO electrodes was studied under CO_2 electroreduction conditions as a model reaction using cyclic voltammetry

[z]E-mail: bogdanoff@helmholtz-berlin.de

(CV) and chronoamperometric (CA) experiments. In order to quantify the effectiveness of the protection layer, the electrochemical surface oxidation of metallic Sn, which can be formed under electrochemically reducing conditions if the films are not sufficiently protected, was measured and monitored using CV measurements. The maximum current is used as a descriptor for the protection ability and its dependence on the deposition parameters was explored. Since metallic Sn particles are active for CO_2 electroreduction, the reaction products are monitored by gas chromatography (GC), mass spectrometry (MS), and ultra-high-performance liquid chromatography (UHPLC). With a pre-deposition FTO etching procedure to smoothen the surface morphology, the Nb:TiO_2-coated FTO electrode exhibited significantly improved electrochemical stability. Meanwhile, the modified FTO electrode still maintains good transparency and conductivity, which makes it a suitable cathode substrate in neutral electrolytes for the investigation of (photo-)electrochemical reactions under reducing conditions.

Experimental

Preparation of Nb:TiO₂/FTO electrodes.—Commercial FTO glass (Pilkington TEC 8) was sliced into 2×2 cm^2 pieces and cleaned in an ultrasonic bath with detergent, acetone, isopropanol, 1 M potassium hydroxide solution, and deionized water (Milli-Q, 18.2 MΩ cm), subsequently. A N_2 gas stream was applied to dry the substrate before use. The deposition of the Nb:TiO_2 layer was performed by direct-current (DC) magnetron sputtering in a custom-made high vacuum chamber with a base pressure of less than 1×10^{-6} mbar. The DC power was set to 100 W and the flow of argon sputtering gas to 23 sccm, which resulted in a discharge voltage of 430 V, a current of 230 mA, and a process pressure of 0.5 Pa. The deposition duration ranged from 42 s to 7 min depending on the desired thickness. The sputtering target was TiO_2-Nb (94/6 at%, Toshima Manufacturing Co., Ltd) with a diameter of 76 mm, which was oriented horizontally, facing upwards, and located 5.5 cm below the downward-facing substrate. A mask is used to avoid coating the edges of the sample so that these uncoated FTO areas can be used to make electrical contact. The schematic of the sputtering process is shown in Fig. S1a. As mentioned in the discussion below, for some selected samples a post-deposition annealing was carried out in a tube furnace at 500 °C with continuous Ar flow for 1 hr.

Pre-deposition FTO etching.—The pre-deposition etching of the FTO substrates was conducted in a customized high vacuum chamber with a base pressure of less than 1×10^{-7} mbar (vario100, scia Systems GmbH), equipped with a horizontally oriented argon ion source. The argon ion beam is striking the substrates at a 45° incident angle. The Ar flow rate was 14 sccm, the operating pressure was 6×10^{-4} mbar, and the applied beam voltage was 300 V with a current of 260 mA. The resulting ion beam density is ~0.38 mA cm^{-2}. The distance between the ion source and the substrate was 28 cm. The substrates were not heated and were rotating at a constant speed of 10 rpm. Etching duration ranged from 5 s to 448 s. The schematic of the process is shown in Fig. S1b.

Electrochemical measurement setup and product analysis.—A custom-made electrochemical cell with a three-electrode configuration was used to perform the electrochemical measurements. The working electrode compartment and the counter electrode compartment were separated by a Nafion 115 membrane and filled with a CO_2-saturated 0.5 M $KHCO_3$ aqueous electrolyte (pH 7.8). We would like to point out that an increase in the local pH value in front of the electrode due to proton consumption cannot be ruled out. Nevertheless, given the low current densities and the intensive mixing of the electrolyte by stirring, this effect is not likely to have a large influence on the results. The sample is mounted as a working electrode at the bottom of the cell. A magnetic stirring bar was used to ensure good mixing of the electrolyte in the working electrode compartment, so that diffusion limitations are minimized. The cell is gas-tight against the surrounding atmosphere and is continuously flushed with CO_2 during the measurement.

For product analysis and gas composition monitoring (avoiding any O_2 contamination), the gas outlet of the cell is coupled to in-line gas chromatography (GC, Thermo Scientific, Trace 1300) and then in the bypass mode to a mass spectrometer (Pfeiffer QMG 250 M1, PrismaPro). The GC was equipped with a thermal conductivity detector (TCD) and a flame ionization detector (FID) with methanizer for sensitive CO and hydrocarbon detection. During the chronoamperometric measurement, the gaseous products were sampled every 13 min by the GC. Parallel to the GC sampling, 1.5 ml of electrolyte was extracted by a syringe for aqueous product analysis and the electrochemical cell was refilled with the same volume of fresh electrolyte. The aqueous samples were analyzed by ultra-high-performance liquid chromatography (UHPLC, Thermo Scientific UltiMate 3000 series) with UV variable wavelength (UltiMate 3000, Dionex) and refraction index (RefractoMax 520, ERC) detectors, and a HyperREZ XP H+ column, using a mobile phase of 5 mM $H_2SO_{4(aq)}$.

A Pt coil serves as counter electrode and a double junction Ag/AgCl reference electrode (REF 451, Radiometer Analytical, filled with 3 M KCl) is placed ca. 1 cm above the center of the working electrode. All the electrochemical experiments were carried out with a Biologic SP-300 potentiostat. The series resistance between the working and reference electrodes was determined by potentiostatic electrochemical impedance spectroscopy (PEIS) at high frequency (usually 10 kHz) before every measurement. The applied potentials in this work have been automatically IR-corrected and converted into the reversible hydrogen electrode scale (RHE) according to the following equation:

$$E_{RHE} = E_{Ag/AgCl} + E^{o}{}_{Ag/AgCl} + 0.059 \times pH + I \times R_{85} \quad [1]$$

where $E_{Ag/AgCl}$ is the applied potential vs the reference electrode (V), E_{RHE} is the potential vs reversible hydrogen electrode (V), $E^{\circ}{}_{Ag/AgCl}$ is the potential of the reference electrode vs NHE (+0.210 V), I is the total current (mA), pH is the pH value of the electrolyte (7.8), and R_{85} corresponds to 85% of the ohmic resistance (determined by PEIS) between working and reference electrode (Ω).

Evaluation of faradaic efficiencies.—The calculation of faradaic efficiency (FE) for gaseous product is as follows:

$$FE_{gaseous\ product}(\%) = \frac{z \times F \times \dot{n}}{i_{total}} \times 100\% = \frac{z \times F}{i_{total}} \times \frac{\dot{V} \times C}{V_M} \times 100\% \quad [2]$$

where C is the concentration of the product measured by GC (v/v), F is the Faradaic constant (96485.33 C mol^{-1}), i_{total} is the averaged current from the time of GC sampling to 3 min prior during electrolysis (A), $\dot{n}$ is the product formation rate (mol s^{-1}), $\dot{V}$ is the CO_2 gas flow rate (8.3×10^{-5} l s^{-1}), V_M is the ideal gas molar volume at room temperature and 1 atm (24.5 l mol^{-1}) and z is the number of electrons transferred for each product molecule (2 for H_2 and CO formation).

The calculation of FE for aqueous product is as follows:

$$FE_{aqueous\ product} = \frac{z \times F \times n}{Q} \times 100\% = \frac{z \times F}{Q} \times C_{HPLC} \times Vol_{cathode} \times 100\% \quad [3]$$

where C_{HPLC} is the concentration of the product measured by UHPLC (mol l^{-1}), n is the quantity of formed product (mol), Q is the total charge that is consumed by the electrolysis process till the

point of aqueous product quantification (C) (i.e., at the 6, 19, 32, and 45 min) and $Vol_{cathode}$ is the volume of the working compartment (L).

Sample characterization.—The morphology of the electrodes was investigated using LEO 1530 Gemini field emission scanning electron microscope (SEM). The SEM images were collected at 3–5 kV acceleration voltage with a 30 μm aperture size and in-lens secondary electron detector. Grazing incidence X-ray diffraction (GIXRD) measurements were performed using a Philips PANalytical X'Pert Pro MRD with Cu Kα radiation (λ = 1.5406 Å) at 40 mA and 40 kV. The angle of incidence was 5° and the measured detection angle (2θ) was varied from 10° to 80° with a step size of 0.01° and a step time of 5 s. UV–vis measurements were performed using a Perkin-Elmer Lambda 950 spectrophotometer in transmittance mode, equipped with an integrating sphere. Prior to measurements, the signals were normalized to 0% and 100% transmission levels without any sample in the beam path. The topography of the samples was measured by atomic force microscope (NT-MDT NovaPX) in semi-contact mode. Then the surface roughness was calculated using the root mean square formula. The scanned area was 1×1 μm^2 with a scan rate of 5 $\mu m\ s^{-1}$. The X-ray photoelectron spectroscopy (XPS) spectra were obtained with a SPECS PHOIBOS 100 hemispherical analyzer using an Al Kα X-ray excitation source ($h\nu \sim 1486.74$ eV). The sample is placed in the analysis chamber pumped down to a base pressure of $\sim 10^{-9}$ mbar. The XPS spectra were acquired using energy steps of 0.05 eV, a dwell time of 0.1 s and a pass energy of 10 eV, with 90 kV and 2200 kV as bias and detector voltages, respectively.

Results and Discussion

Stability of bare FTO under CO_2 electrolysis conditions.—To characterize the electrochemical stability of unprotected FTO, electrolysis experiments were carried out in a pH-neutral electrolyte (continuously CO_2-purged 0.5 M $KHCO_3$, pH 7.8) under a constant potential of −0.74 V_{RHE} for about 45 min. Every 13 min, the gaseous and water-soluble products were analyzed by GC and UHPLC. The same electrolyte volume extracted for UHPLC analysis was immediately replenished by injecting fresh electrolyte into the electrochemical cell.

As depicted by the black line in Fig. 1a, the overall current density is increasing with electrolysis time, which indicates a change in the activity of the electrode. The violet diamonds represent the timing for the product sampling. After product sampling, the sharp decrease in the overall current density is due to a short-term reduced concentration of the dissolved CO_2 in electrolyte, as the fresh electrolyte was not pre-saturated with CO_2. This observation offers a first hint that the observed overall current is associated with electrochemical CO_2 reduction. Indeed, product analysis by GC and UHPLC reveal CO and $HCOO^-$ formation and an omnipresent hydrogen evolution reaction (HER) as shown in Fig. 1b. No other products were identified within our experimental conditions. Since FTO itself is not active for CO_2 reduction, the activity likely originated from the metallic tin that was formed during electrochemical reduction of FTO. Grazing incidence X-ray diffraction (GIXRD) data of the bare FTO electrode after electrolysis indeed shows a distinct metallic Sn pattern in Fig. 1c, which is not observed on the pristine FTO. Moreover, the scanning electron microscopy (SEM) image shows distinct changes from a clear crystalline structure to a homogeneous distribution of particles in the form of dendrites (see Fig. S2).

The calculated partial current densities and faradaic efficiencies for the respective products in Figs. 1a, 1b reveal formate and hydrogen as main products accompanied by a minor amount of CO. Although the total current density kept increasing during the 45-min electrolysis, no clear trend and a nearly unchanged distribution of products are observed. Averaged over the entire electrolysis time, 50% of the current is used for the reduction of CO_2, while around 40% contributes to the HER. The remaining 10% of the current cannot be assigned to any product that can be detected by GC or UHPLC. Part of this 10% is likely used for the corrosion of FTO, i.e., SnO_x reduction to metallic Sn.[14] However, 10% of the total charge would lead to a complete dissolution of the FTO layer, whereas the GIXRD results shown in Fig. 1c still show a clear FTO pattern after 45 min of electrolysis. From this we roughly estimate that at most 3%–5% of the current is used to reduce FTO to metallic Sn. There are seemingly other minor electrochemical processes occurring, that we are unable to assign. The product distribution is consistent with publications showing that metallic tin reduces CO_2 predominantly to $HCOO^-$ and only a small portion to CO and H_2. However, the HER formation in our study is significantly higher than the reported value for a pure tin electrode.[57] To examine the transient H_2 formation rate, a chronoamperometry experiment combined with MS was conducted, which has a faster response time than GC. The results, shown in Fig. S3, reveal that HER already occurs at the very beginning of the electrolysis experiment, where the amount of reduced Sn particles is still negligible. Thus, the FTO surface itself appears to be active for the HER. The initial faradaic efficiency of only ∼65% for HER, however, indicates that this reaction competes with the electrochemical reduction of Sn. The faradaic efficiency of H_2 quickly levels off to 40% with proceeding electrolysis due to increasing competition from CO_2 reduction at the formed tin particles. This final value corresponds well to the results of the GC measurements at longer electrolysis times.

These results show that bare FTO is not a suitable substrate for investigating electrochemical reduction reactions due to its poor electrochemical stability. The electrochemical activity of the formed metallic Sn will always interfere and distort the investigation of any catalyst deposited onto the FTO (unless the catalyst completely covers the FTO and prevent it from being exposed to the electrolyte, which is often difficult to achieve). Furthermore, the appearance of the electrode became noticeably darker after electrolysis (Fig. 2c). The electrode transparency at 550 nm plummeted to 3.9% compared to 75.3% for pristine FTO. This will greatly hinder further photoelectrochemical or other spectroscopic investigations. These findings clearly illustrate the need to prevent the FTO from coming into direct contact with the electrolyte.

Sputtered Nb:TiO_2 protection layer on top of FTO.—To protect the FTO films against electrochemical reduction, Nb-doped TiO_2 films with a thickness of 10 to 100 nm were deposited onto the FTO by DC magnetron sputtering. To obtain a descriptor that allows monitoring the reduction of FTO and thereby studying the effectivity of the protection layers, CV measurements were employed. The results for an unprotected FTO electrode are depicted in Figs. 2a, 2c, while the results for protected FTO samples are shown in Figs. 2b, 2d. The full-range CV cycles up to −1.4 V_{RHE} can be seen in the supporting information (Fig. S4).

In general, the anodic and cathodic peaks observed in the CV measurements on the bare FTO electrode arise from the redox chemistry of metallic Sn particles formed during FTO corrosion (Figs. 2a, 2c). The reduction of the highly crystalline SnO_x of the FTO electrode occurs at potentials more negative than −0.6 V_{RHE} and is obscured by the prevailing HER, rendering it indiscernible in the CV cycles (see Fig. S4). The hydrogen formation was confirmed by both MS and GC. The redox chemistry of metallic Sn has already been extensively discussed in the literature, which is used for assigning the peaks observed in our CV experiments.[58–70] The first anodic peak at −0.087 V_{RHE} in Figs. 2a, 2c can be assigned to the surface oxidation of metallic Sn particles to thin layers of $Sn(OH)_2$ or SnO, while the more positive peak at +0.08 V_{RHE} represents the further oxidation to $Sn(OH)_4$ or SnO_2.[70] The broad anodic wave at +1.14 V_{RHE} is assigned to anodic oxide growth into thicker surface layers, which is a typical characteristic of valve metals.[65,69] The cathodic peak at −0.53 V_{RHE} indicates the reduction of these thin Sn oxide surface layers back to metallic Sn. Since these oxidized Sn particles are absent at the pristine, uncorroded FTO surface, no

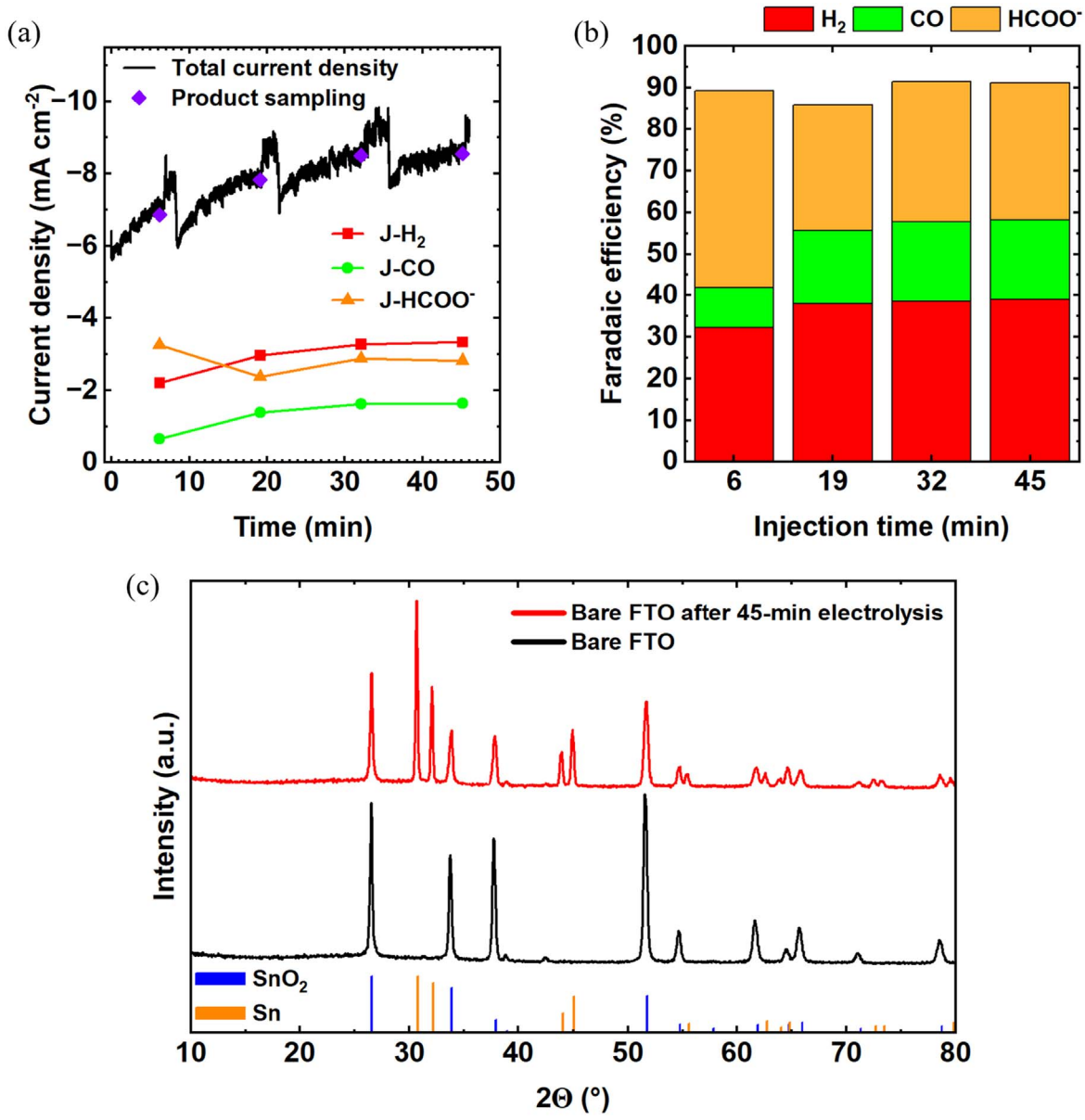

Figure 1. (a) Time-dependent current density and (b) the corresponding faradaic efficiencies on bare FTO at -0.74 V_{RHE}. (c) Grazing incidence X-ray diffraction (GIXRD) pattern of the bare FTO, before and after 45-min electrolysis at -0.74 V_{RHE}. Electrolyte: CO_2-purged 0.5 M $KHCO_3$ (pH 7.8). CO_2 flow rate: 5 ml min^{-1}. The violet diamonds represent the timing for gaseous and aqueous products sampling by on-line GC and UHPLC.

cathodic peak is observed during the first cathodic scan in Fig. 2a. With increasing number of CV cycles, both the anodic peaks and the cathodic peak at -0.55 V_{RHE} grow bigger. This suggests that with each cathodic scan to potentials negative of -0.6 V_{RHE}, more and more metallic tin particles are accumulating on the FTO surface, which in turn lead to a growing anodic oxidation peak and a growing cathodic reduction peak at -0.55 V_{RHE} (during which the surface oxides are reduced again). Thus, the Sn redox peaks serve as descriptors of the FTO corrosion progression. By plotting the peak current density of the first anodic peak at -0.087 V_{RHE} (indicated by the star symbol in Fig. 2a) as a function of cycle number, the ongoing FTO corrosion trend is clearly revealed (Fig. 2c).

The newly found corrosion descriptor is then utilized to investigate the effectivity of the Nb:TiO_2 protection layer. Nb:TiO_2 film thicknesses of 10 nm, 20 nm, 50 nm, and 100 nm were deposited with DC magnetron sputtering and investigated. Top-view and cross-sectional SEM images of the 100 nm Nb:TiO_2 film on FTO are shown in Figs. S5a, S5b. The films appear almost identical to bare FTO, which illustrates the excellent homogeneity and conformal nature of the Nb:TiO_2 protection layers. The Nb:TiO_2 layers are mainly amorphous as no distinct diffraction pattern of crystalline TiO_2 was observed in the GIXRD pattern (green curve in Fig. S5c).

Figure 2b depicts the first out of ten CV cycles on protected FTO samples with different Nb:TiO_2 layer thicknesses. For the sake of clarity, only the first cycle is shown to demonstrate the immediate influence of the Nb:TiO_2 protection layer. The whole CV series of each sample can be seen in Fig. S6. The curves in Fig. 2b appear slightly different than the bare FTO, as the electrochemical response is now affected by amorphous Nb:TiO_2. One difference is the significantly increased pseudo-capacitance in the potential range from 0 to -0.7 V_{RHE}, which is due to the presence of Nb:TiO_2.[71–74] As can be seen in Fig. 2b, the forward scan intersects with the reverse scan at approximately -0.8 V_{RHE}. Based on the findings in literature, we hypothesize that this phenomenon may be attributed to the formation of a Ti^{IV}/Ti^{III} redox couple in TiO_2.[35–37] Because of

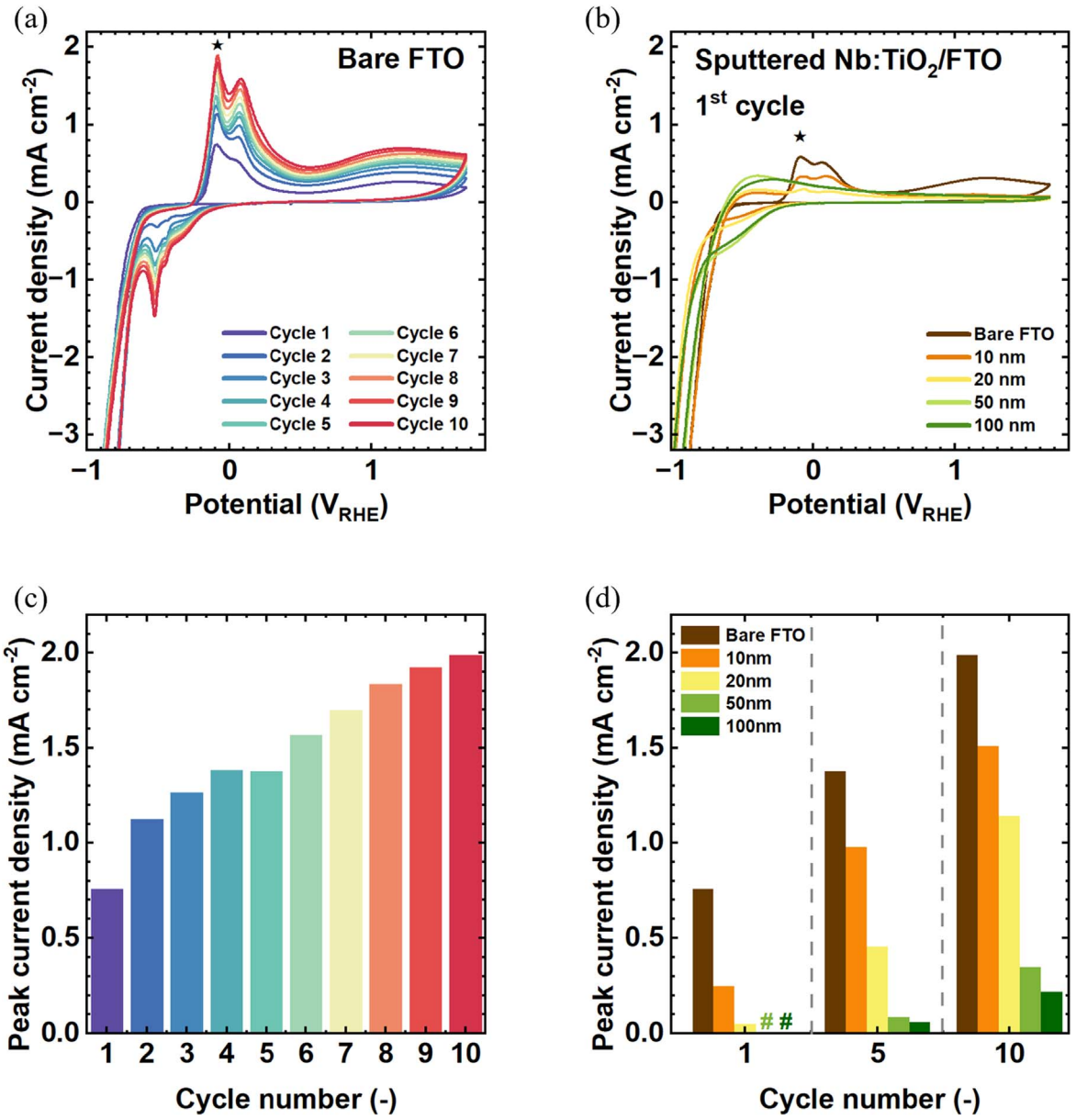

Figure 2. (a) Cyclic voltammetry and (c) the peak current of the tin reoxidation peak, marked by the star symbol in (a), of bare FTO (TEC 8) in the electrochemical CO_2 reduction region. (b) Cyclic voltammetry (only the 1st cycle) and (d) the peak current of the tin oxidation peak, marked by the star symbol in (b) of sputtered Nb:TiO_2/FTO electrodes in the electrochemical CO_2 reduction region (for various Nb:TiO_2 thicknesses: 0, 10, 20, 50, and 100 nm). Electrolyte: CO_2-saturated 0.5 M $KHCO_3$ (pH 7.8). Scan rate: 50 mV s^{-1}. The number signs serve as placeholders for negligible peak current values in (d). The peak current was obtained after subtracting the baseline for each individual CV cycle.

the enhanced catalytic activity of these centers, the reverse scan exhibits a higher current than the forward scan. The intersection of the two curves at lower overpotentials (associated with smaller faradaic currents) corresponds to the capacitive contribution to the total current. More importantly, the current density of the anodic peak (indicated by the star symbol in Fig. 2b) decreases rapidly with increasing Nb:TiO_2 layer thickness, as illustrated in Fig. 2d. For the 1st cycle, 10 nm of sputtered Nb:TiO_2 leads to a 67.2% reduction in peak intensity compared to the bare FTO, and for layers thicker than 20 nm, there is virtually no Sn oxidation peak. For protection layers of 20 nm and above, corrosion becomes only visible from the 5th cycle. Even at the 10th cycle, 100 nm of sputtered Nb:TiO_2 suppresses the oxidation peak by 89% compared to the bare FTO sample. It is evident that the sputtered Nb:TiO_2 layer effectively impedes FTO corrosion. Nevertheless, the Sn oxidation peak is gradually emerging over time, which indicates that the reduction of the FTO to metallic tin still occurs, albeit at a significantly lower rate.

It is well known that annealing is an effective method to enhance the conductivity and the stability of the TiO_2 layer by inducing crystallization to anatase or rutile structures.[31,47,75–77] Thus, post-deposition annealing of the Nb:TiO_2-coated FTO substrates at 500 °C in Ar for 1 hr was carried out in a quartz tube furnace. However, the CV measurements in Fig. S7 show that the annealing seems to cause more pronounced pinhole formation across the surface, as the tin reoxidation peak intensity becomes more prominent compared to the non-annealed sample. Further studies on the post-deposition annealing treatment were therefore not pursued.

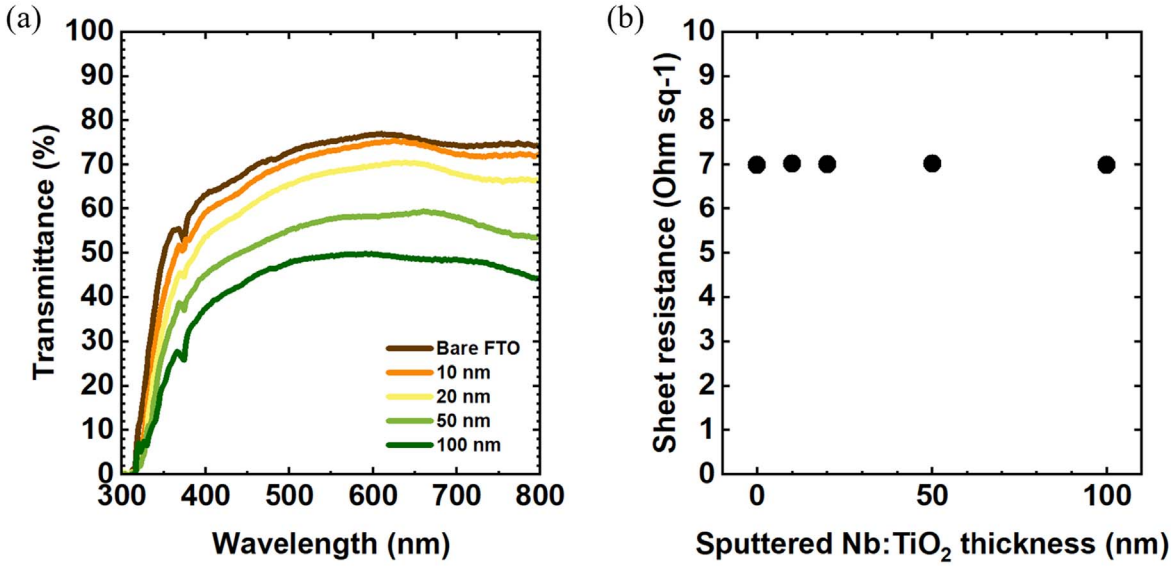

Figure 3. (a) Transmittance curves obtained by UV–vis measurement and (b) sheet resistance obtained by four-probe measurement of the sputtered $Nb:TiO_2$/FTO electrodes for various $Nb:TiO_2$ film thicknesses.

Transmittance and conductivity of the Nb:TiO$_2$/FTO samples.—Since low optical loss is one of the crucial characteristics of an ideal substrate in photoelectrochemical research, it is important to consider the transparency of the protective layers. Figure 3a shows that the transmittance decreases significantly with increasing layer thickness of the $Nb:TiO_2$. Despite this, a transmittance of 45% in the spectral region between 500–700 nm for the 100 nm $Nb:TiO_2$/FTO sample would still suffice for spectroscopic or PEC studies.

Another important parameter of the protective layer is its conductivity. In order not to limit the charge transport from the FTO substrate to the electrolyte interface, a high conductivity is desirable. The sheet resistance of the $Nb:TiO_2$/FTO samples was determined by an automatic four-point probe meter. The data in Fig. 3b shows that regardless of the thickness of the protection layers, all samples show almost the same value as uncoated FTO glass. Although the measuring contacts are located on top of the $Nb:TiO_2$ layer, the overall sheet resistance is seemingly determined by the underlying FTO. This can be explained by the fact that the lateral sheet resistance of the protective $Nb:TiO_2$ layer is significantly higher than that of the FTO. Note that the resistance of the protection layer in the direction perpendicular to the surface is comparatively small and negligible owing to the very thin layer thickness. This is also confirmed by the slopes of the CV curves of bare and protected FTO samples, which show approximately the same values (ca. 25 Ohm at -15 mA cm^{-2} in Fig. S4b). The protective layer therefore does not seem to significantly affect the conductivity of the TCO substrate under the current experimental conditions.

CO$_2$ reduction with 100 nm Nb:TiO$_2$/FTO electrodes.—Since they showed the best stability, 100 nm thick $Nb:TiO_2$ layers were chosen for extended electrolysis experiments to further investigate their effectivity. The measurements were carried out analogous to the electrolysis experiments on uncoated FTO shown above.

In Fig. 4a, the total current density for the 100 nm $Nb:TiO_2$-protected FTO still increases gradually with time from -1.4 mA cm^{-2} to -2.5 mA cm^{-2}. The main product throughout the electrolysis is hydrogen, which starts with a faradaic efficiency of 90% and drops down to 60% when other competitive reactions gradually emerge. The total current is about 75% smaller than for the unprotected FTO (Fig. 1a). This can be explained by the effective suppression of corrosion, which leads to noticeably less electrochemically reduced metallic Sn particles. As a result, the rate of CO_2 reduction reactions is much smaller, since $Nb:TiO_2$ is a much poorer CO_2 reduction catalyst than metallic Sn. This also explains why the pronounced drop in current that is observed in Fig. 1 after taking GC/UHPLC samples no longer occurs in Fig. 4; since no CO_2 reduction occurs at the $Nb:TiO_2$ surface, the absence of CO_2 in the solution that is added to replenish the electrolyte does not affect the current. As shown in Fig. 4b, formate formation is completely suppressed at the beginning of the experiment. Only after 19 min of electrolysis, a trace amount of formate is detected. The faradaic efficiency of formate increases slightly with time to 6% at the end of 45 min. Still, it is substantially smaller than the 33% measured for a bare FTO electrode. A lower faradaic efficiency of CO formation is also observed.

The fraction of the current that could not be attributed to any product formation is seemingly much higher for the protected FTO than for the bare FTO. This current is believed to be partially consumed by the FTO corrosion process. After 45 min of electrolysis, it is around 25% on the protected FTO compared to 10% on the bare FTO. This discrepancy can be explained by the different initial states of the electrodes. For the bare FTO, the entire surface is exposed to corrosion from the beginning and the corrosion would quickly reach a steady state. On the other hand, for the protected FTO, the corrosion only begins slowly from a handful of tiny pinholes. In the beginning, this corrosion current is quite inconsequential compared to the dominant HER. However, with the electrolysis progression, the corrosion rate increases rapidly through more exposed areas from the pinholes. Consequently, the faradaic efficiency of corrosion rises steadily. In addition, HER at the $Nb:TiO_2$ protective layer is significantly less efficient than at the bare FTO, so the fraction of corrosion in the total current is higher.

The results show that 100 nm sputtered $Nb:TiO_2$ layer can protect the FTO to a large extent, but it cannot fully prevent FTO corrosion during 45 min of electrolysis. This is confirmed by the presence of a series of small peaks indicating the presence of metallic Sn in the post-mortem GIXRD pattern shown in Fig. 4c. Pinholes across the protective layer are most likely responsible for the corrosion. Interestingly, protection layers deposited on very smooth surfaces, such as wafer-based materials, seem to offer much better protection.[28–33,48,51,53–55] Since the commercially available FTO substrates used in this study possess a relatively rough surface

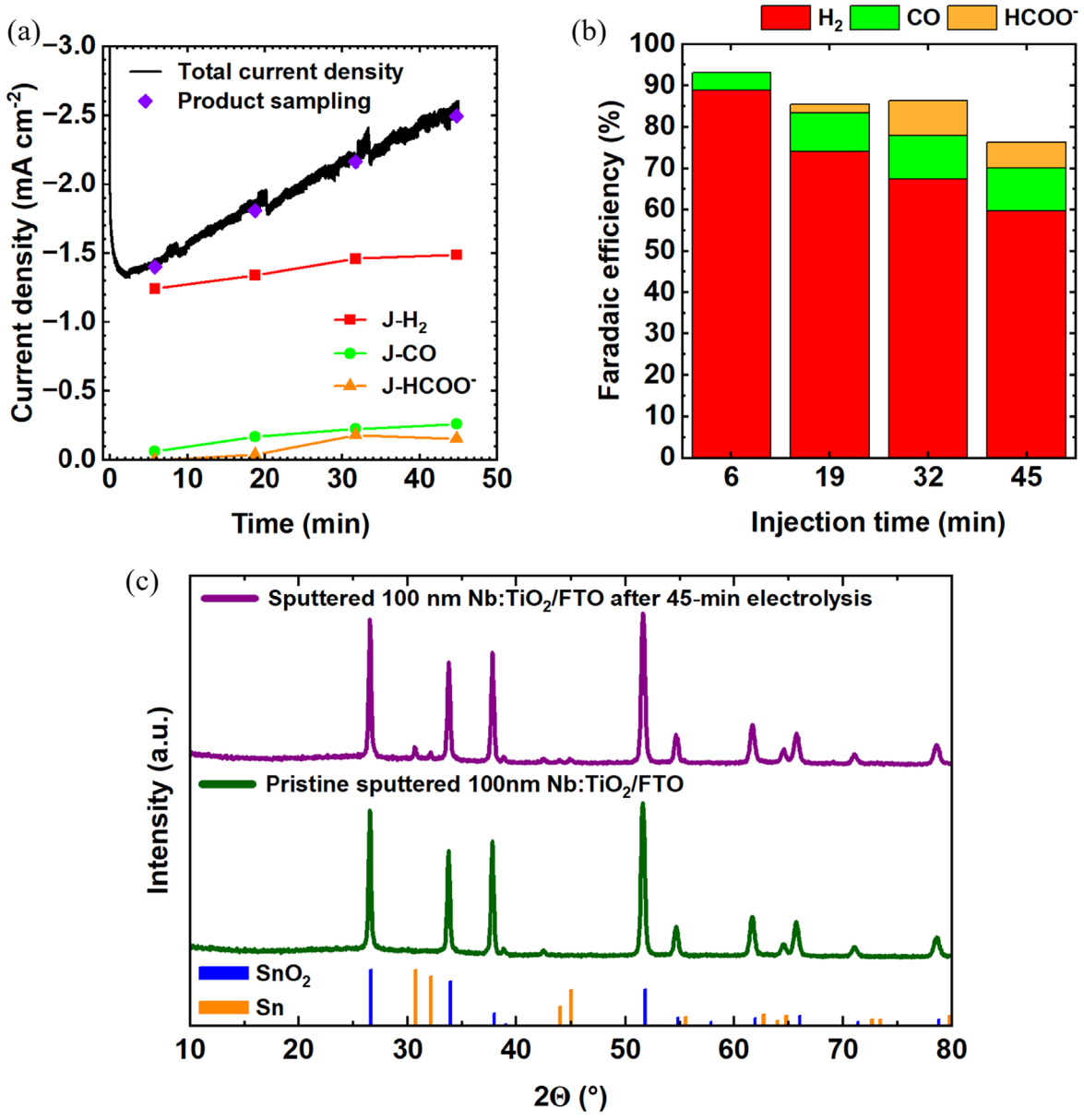

Figure 4. (a) Time-dependent partial and total current densities and (b) the corresponding faradaic efficiencies on sputtered 100 nm Nb:TiO_2/FTO at −0.74 V_{RHE}. (c) GIXRD patterns of 100 nm Nb:TiO_2/FTO, before and after 45-min electrolysis at −0.74 V_{RHE}. Electrolyte: CO_2-saturated 0.5 M $KHCO_3$ (pH 7.8). CO_2 flow rate: 5 ml min^{-1}. The violet diamonds represent the sampling moments by on-line GC and UHPLC.

morphology, it seems likely that these pinholes are mainly located at the tips and edges of the FTO crystallites. Hence, the next step is to try smoothening the FTO surface before depositing the Nb:TiO_2 protective layer. This should result in fewer pinholes across the Nb:TiO_2 layer, which would then enhance the electrochemical stability of the electrode.

Pre-processing FTO by ion beam etching.—To smoothen the surface of pristine FTO, an argon ion etching step is used before depositing the protection layer. The etched FTO will be denoted as FTO* in the remainder of the manuscript. The duration of the etching process was varied between 8 and 448 s, resulting in different degrees of FTO ablation.

Cross-sectional SEM images in Fig. 5a show that the FTO surface becomes smoother, and the FTO film thickness thinner, with increasing etching duration. Owing to the constant ablation rate of the process, the reduction in FTO film thickness depends linearly on etching time (see Fig. S8). The root mean square value of the surface roughness (R_{RMS}) was determined by atomic force microscopy (AFM) and exhibits a sizeable reduction from 35.4 nm (pristine TEC 8 FTO) to 20.6 nm (FTO*448 s). The details can be seen in Fig. S9. Apparently, most of the critical tips and edges of the FTO crystals were removed by the etching process, which results in a smoother surface morphology. This effect can also be observed from the top-view SEM images in Figs. 5b, 5c. The results demonstrate that this etching method has achieved what we intended to.

After the deposition of Nb:TiO_2 on various FTO* substrates, the electrochemical stability, transparency, and conductivity were investigated in the same way as above. The transmittance of the Nb:TiO_2/FTO* samples does not seem to be critically affected by the FTO etching process, as illustrated in Fig. 6a. Although the Nb:TiO_2/FTO* electrodes seem to show a slightly higher transmission compared to the non-etched one, no clear trend between the etching time and electrode transmission could be observed. All

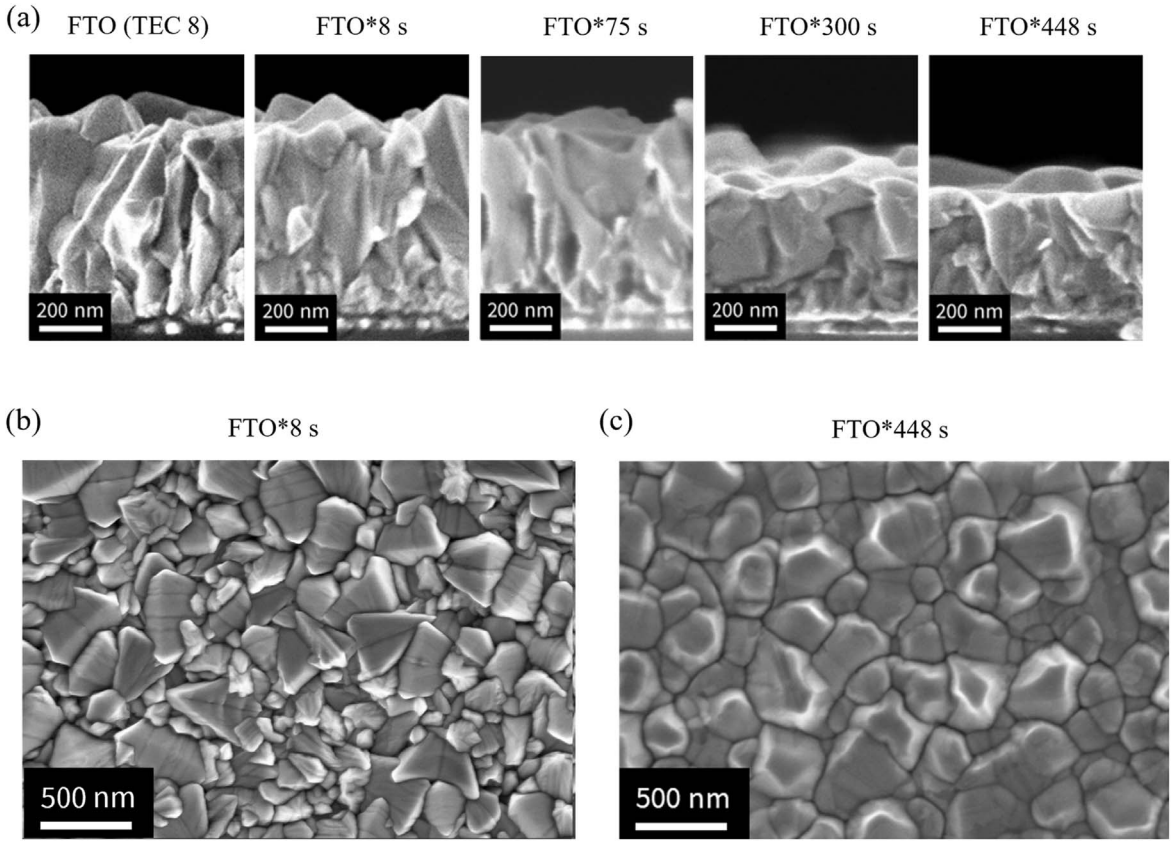

Figure 5. (a) Cross-sectional SEM images of FTO with increasing etching duration (from 0, 8, 75, 300 to 448 s). Top-view SEM images of the (b) FTO after 8 s etching and (c) FTO after 448 s etching.

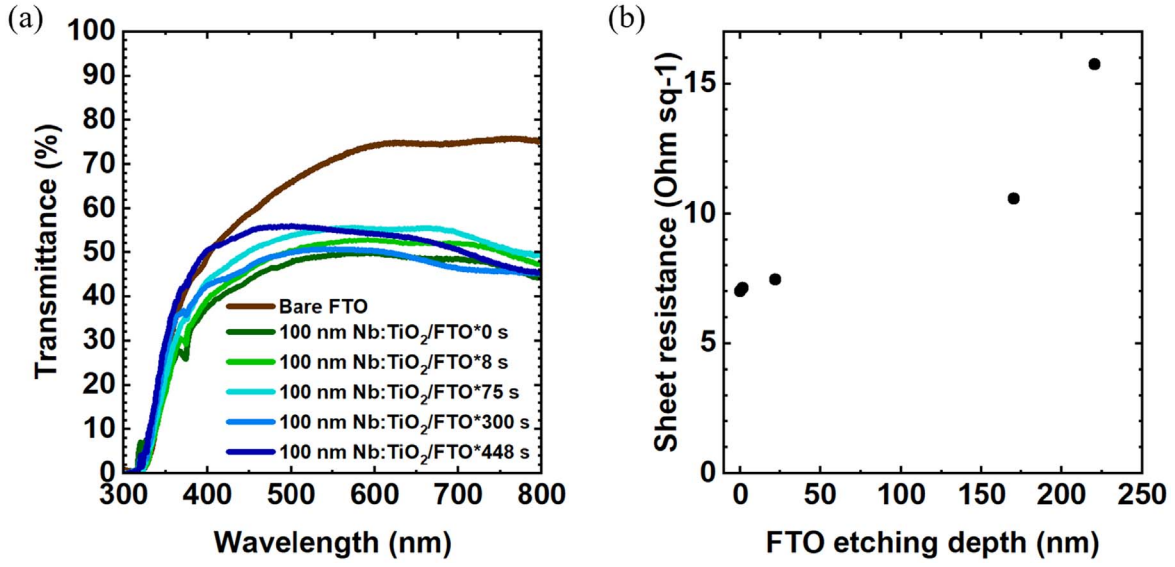

Figure 6. (a) Transmittance curves obtained by UV–vis measurement and (b) sheet resistance obtained by four-probe measurement of the sputtered 100 nm Nb:TiO_2/FTO* samples (for various FTO etching time: 8, 75, 300, and 448 s).

samples show approximately the same transmission curve with a minor variance. Compared to the bare FTO, the main transmittance loss stems from the 100 nm Nb:TiO_2 layer.

As expected, four-point conductivity measurements reveal that the sheet resistance of the Nb:TiO_2/FTO* samples increases with FTO etching duration, as shown in Fig. 6b. The in-plane resistance of the underlying FTO increases with decreasing layer thickness. This once again confirms the assumption mentioned above that the sheet resistance of the Nb:TiO_2/FTO* samples is mainly determined by the lateral conductivity of the FTO* underneath the protective

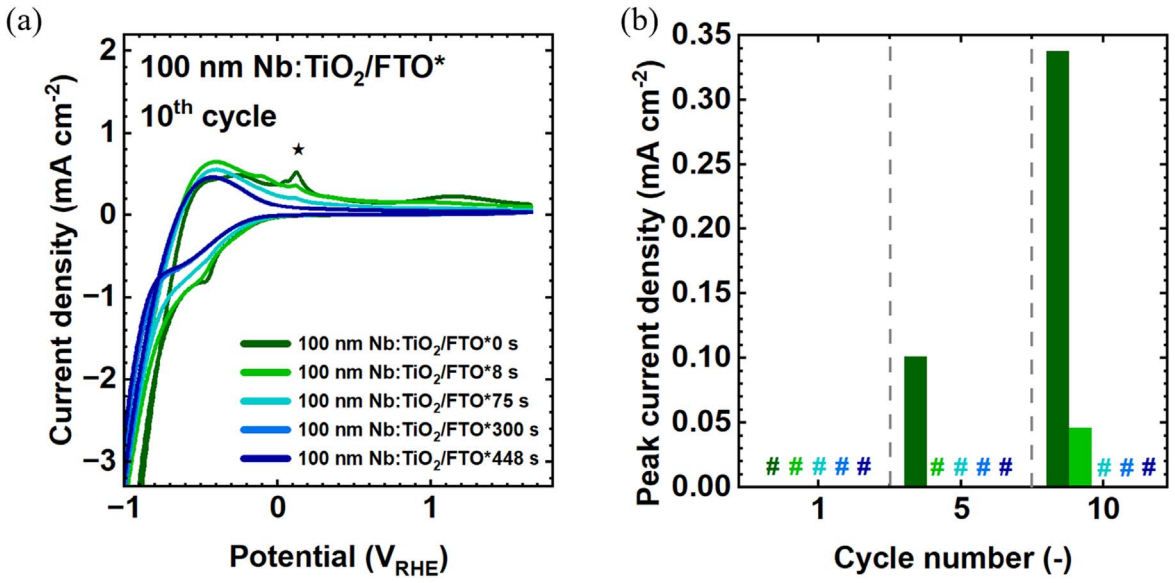

Figure 7. (a) Cyclic voltammetry (the 10th cycle) and (b) the tin-reoxidation peak current (marked by the star symbol) of the 100 nm Nb:TiO_2/FTO* electrodes for various FTO etching times during electrochemical CO_2 reduction. Electrolyte: CO_2-saturated 0.5 M $KHCO_3$ (pH 7.8). Scan rate: 50 mV s^{-1}. The number signs serve as a placeholder for values that are too small to distinguish in the graph. The peak current was obtained after subtracting the baseline for each individual CV cycle.

layer. In this respect, it must be considered that there is a trade-off between the surface roughness and the electrode conductivity, which should be adjusted according to the particular requirements.

The electrochemical stability of the Nb:TiO_2/FTO* substrates was analyzed analogous to the measurements described above using CV and CA. The results from CV measurements in Fig. 7a reveal a clear stability improvement of the etched samples over the non-etched one. The evaluation of the Sn reoxidation peak (labeled by the star symbol in Fig. 7a) is plotted in Fig. 7b. It shows that at the 1st cycle, all samples, including the etched and non-etched ones, have no detectable Sn reoxidation peak, which indicates no or negligible corrosion. At the 5th and 10th cycle, the non-etched sample shows significant signs of corrosion. In comparison, all etched samples remain stable and show no evidence of corrosion, except for the sample etched for the shortest time (Nb:TiO_2/FTO*8 s). For this sample, a small peak current could be observed at the 10th cycle (light-green column in Fig. 7b). The smoothing of the FTO substrate by ion etching clearly enhances the electrochemical stability of the protection layer and can completely suppress FTO corrosion in our CV stability experiments.

The considerably improved electrochemical stability was confirmed with chronoamperometry experiments under CO_2 electrolysis conditions. Figure 8a shows that even a relatively short FTO etching process of 75 s leads to complete stabilization of the Nb:TiO_2/FTO* electrode during 45 min of electrolysis. While hydrogen is the main product with a faradaic efficiency of over 95%, no formate production could be detected by UHPLC. This clearly indicates the absence of metallic Sn and, therefore, the absence of FTO corrosion. The GIXRD patterns in Fig. 8c indeed show no sign of metallic tin. The very small fraction of CO formation during electrolysis can probably be attributed to the minor activity of the Nb:TiO_2 layer.

The top-view SEM images in Figs. 9a, 9b display no substantial structural changes to the electrode surface after the 45-min electrolysis experiment. Moreover, Ti 2p and Nb 3 d XPS spectra of the Nb:TiO_2/FTO*300 s electrode reveal no significant changes after 45-min of electrolysis, as seen in Fig. S10. This observation verifies the chemical stability of the Nb:TiO_2 layer under CO_2-electrolysis conditions. It should be noted at this point that the absence of Ti^{III} species after electrolysis in the XPS analysis could be possibly attributed to the ambient air exposure between the electrochemical experiments and the XPS measurements. The Ti^{III} centers, which are reported to form under cathodic (over)potentials due to the reduction of Ti^{IV} species, are likely reoxidized to Ti^{IV} during sample storage and transfer. Furthermore, the transmittance curve of the electrode is practically unchanged after electrolysis, as shown in Fig. 9c.

To explore the limits of the optimized protective layer, a longer CO_2-electrolysis experiment on the 100 nm Nb:TiO_2/FTO*300 s electrode for approximately 210 min was conducted and the corresponding time-dependent current densities are shown in Fig. S11. Throughout the 210 min of electrolysis, H_2 was observed as the predominant gaseous product, showing a faradaic efficiency exceeding 97%. A minor amount of CO was detected, corresponding to a FE below 3%. The formation of HCOOH, a main descriptor for FTO corrosion, was detected only at the end of the electrolysis with a FE of less than 1%. These results indicate that no FTO corrosion can be detected within our detection capabilities during the approximately 210 min electrolysis period. However, the CO partial current density began to increase after approximately 90 min, which might suggest the onset of structural changes in the Nb:TiO_2 protection layer. As a possible failure mechanism of the Nb:TiO_2 protection layer, we propose that mechanical stress imposed by the gas bubble evolution at the surface may induce microscopic structural defects (e.g., pinholes or microfractures) during prolonged operation.

Overall, our results show that sputtered Nb:TiO_2 layers can effectively suppress the FTO corrosion process, making them a possible alternative for frequently used ALD-TiO_2 protective coatings. The prerequisite is a homogeneous and conformal coverage of the protective layer; otherwise, corrosion would still occur and spread via the pinholes and cracks. Here, ALD has a distinct advantage over sputtering technology, especially for substrates with a rough morphology. However, if large quantities of samples are required, then the sputtering technique appears to be more attractive because of its relatively facile and cost-effective operation. Especially in the initial stage of catalyst screening, it is advantageous to first examine the deposition parameters of the catalyst layer on sputtered protection layers. Subsequently, the optimized set of parameters can be transferred to the ALD layers, thereby potentially expediting the catalyst development process. Due to the rough

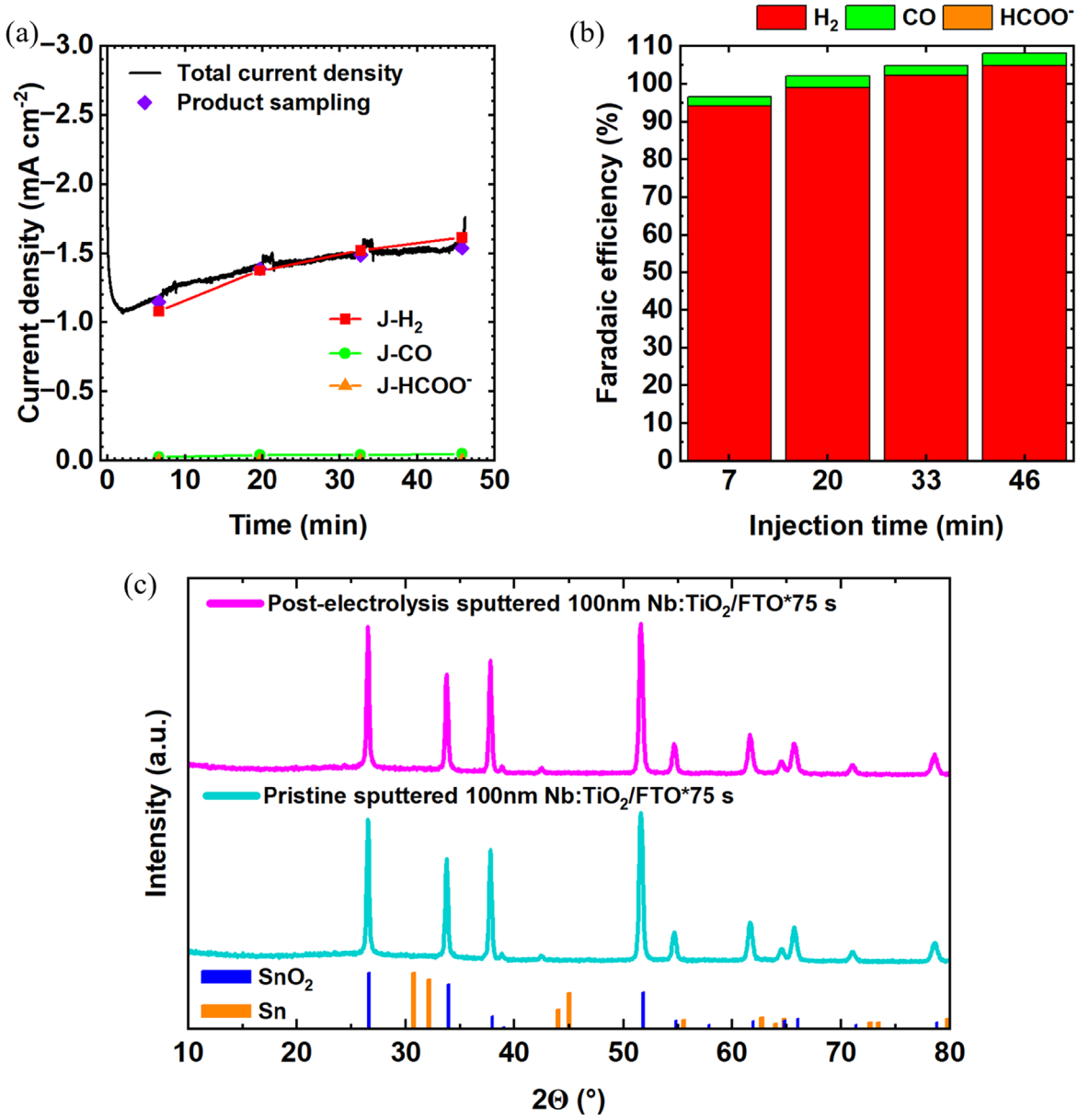

Figure 8. (a) Time-dependent current density and (b) the corresponding faradaic efficiencies for 100 nm Nb:TiO_2/FTO*(75 s) at −0.74 V_{RHE}. (c) GIXRD pattern of the 100 nm Nb:TiO_2/FTO*75 s samples before and after 45-min electrolysis at −0.74 V_{RHE}. Electrolyte: CO_2-saturated 0.5 M $KHCO_3$ (pH 7.8). CO_2 flow rate: 5 ml min^{-1}. The violet diamonds represent the timing for gaseous and aqueous products sampling by on-line GC and UHPLC.

surface topography of commercial FTO/glass substrates, achieving a truly conformal coverage with DC magnetron sputtering turned out to be challenging. This, however, can be alleviated by etching the FTO substrate with an argon ion beam to smoothen the surface before depositing the protection layer. We demonstrated that this procedure can stabilize the commercial FTO substrates under CO_2 reduction conditions in neutral electrolyte at moderate cathodic overpotential for 45 min. Moreover, the protected FTO substrates maintain good optical transmittance and good electrical conductivity after applying the protection layer.

Conclusions

This work demonstrates how commercial FTO-coated glass electrodes can be protected against corrosion under electrochemically reducing conditions. For our investigations, we chose electrochemical CO_2 reduction (CO_2-electrolysis) in a pH-neutral electrolyte at moderate cathodic potentials as a model reaction. We show that bare FTO suffers from strong electrochemical corrosion, which leads to the formation of metallic tin and thereby to optical transparency losses. The CO_2 reduction activity of these metallic tin particles can be used as an indicator for FTO corrosion. We demonstrated that the deposition of thin Nb:TiO_2 films on top of commercial FTO glass by DC magnetron sputtering can suppress corrosion to a large extent. Eventually, however, corrosion still gradually occurs through pinholes or cracks in the protection layer. The electrochemical oxidation of surface tin particles, which are formed during the corrosion process, can serve as a descriptor for the effectiveness of the protection layer. A dramatic improvement of the corrosion protection can be achieved by smoothening the FTO surface using argon ion beam etching prior to deposition of the Nb:TiO_2 protection layer. Optimization of the process parameters resulted in a conductive Nb:TiO_2-covered FTO substrate that shows no electrochemical corrosion during 45 min of CO_2-electrolysis at −0.74 V_{RHE} in 0.5 M carbonate buffer (pH 7.8). This highly

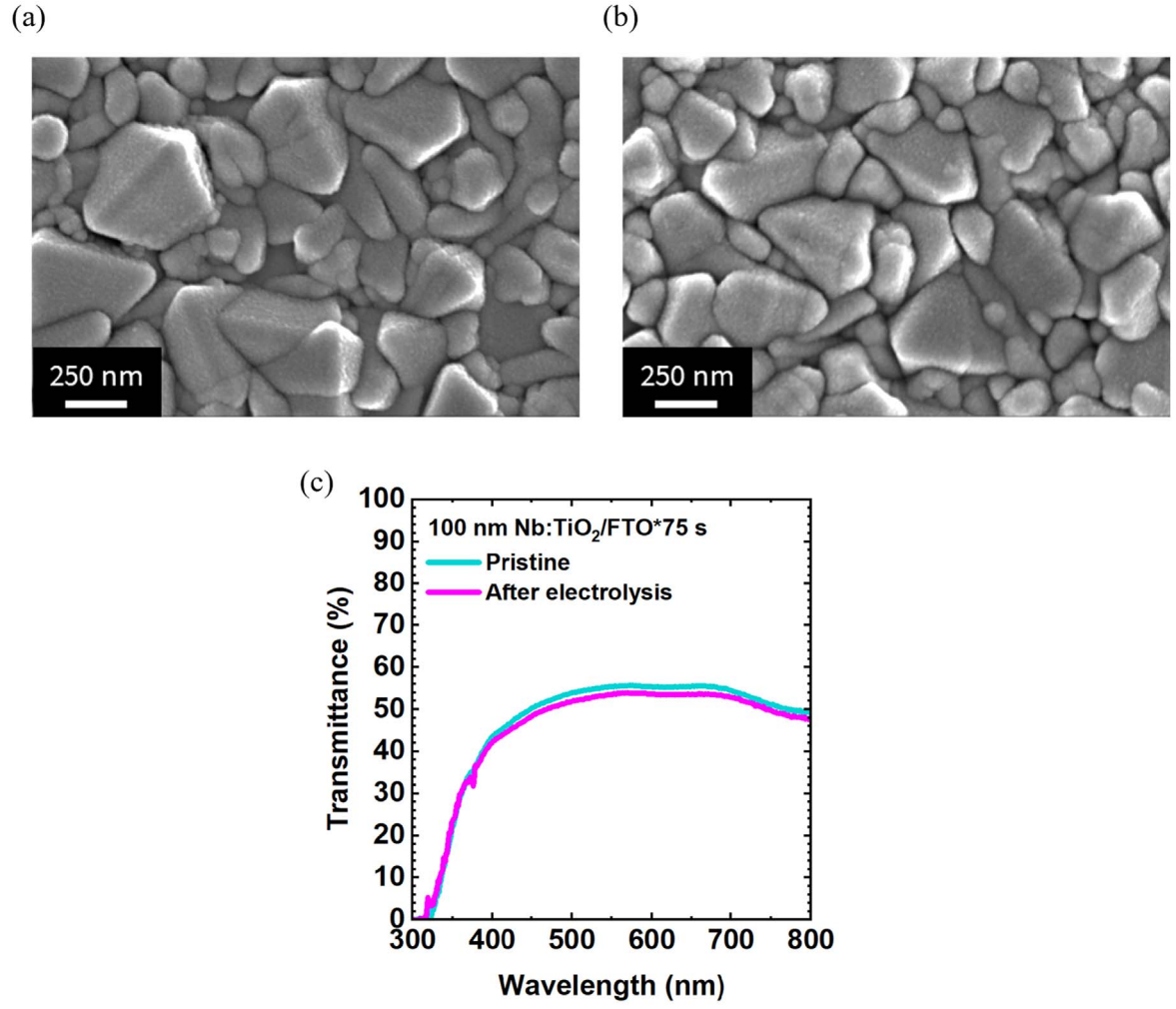

Figure 9. Top-view SEM images of 100 nm Nb:TiO_2/FTO*(75 s) samples (a) before and (b) after electrolysis. (c) Optical transmittance curves of the samples before and after electrolysis. Electrolysis was performed at -0.74 V_{RHE} for ca 45 min. Electrolyte: CO_2-saturated 0.5 M $KHCO_3$ (pH 7.8). CO_2 flow rate: 5 ml min^{-1}.

effective protection strategy enables the use of commercial FTO substrates as convenient, low-cost electrodes for electrochemical studies at cathodic potentials, i.e., under strongly reducing conditions. An optical transparency of around 53% and a sheet resistance comparable to that of regular FTO makes these substrates highly suitable for photoelectrochemical or spectro-electrochemical investigations.

Acknowledgments

The authors sincerely thank Klaus Schwarzburg for his support with the AFM measurements. The authors also thank Christian Höhn for this support with the XPS measurements. This work is funded by the German Federal Ministry of Education and Research (BMBF), project "DEPECOR" (FKZ: 033RC 021C). The authors like to thank the Helmholtz-Center Berlin for technical and additional financial support.

ORCID

Yu-Lin Tsai https://orcid.org/0000-0003-1219-8352
Karsten Harbauer https://orcid.org/0000-0002-2346-8146
Siddharth Gupta https://orcid.org/0000-0001-6139-8604
Matthew T. Mayer https://orcid.org/0000-0001-5379-2775
Roel van de Krol https://orcid.org/0000-0003-4399-399X

References

1. G. K. Dalapati et al., *J Mater Chem A Mater*, **9**, 16621 (2021).
2. H. Wen, B. Weng, B. Wang, W. Xiao, X. Liu, Y. Wang, M. Zhang, and H. Huang, *Nanomaterials*, **14**, 591 (2024).
3. M. Powalla, S. Paetel, E. Ahlswede, R. Wuerz, C. D. Wessendorf, and T. Magorian Friedlmeier, *Appl. Phys. Rev.*, **5**, 041602 (2018).
4. J. E. Ikpesu, S. E. Iyuke, M. Daramola, and A. O. Okewale, *Sol. Energy*, **206**, 918 (2020).
5. G. Nandan Arka, S. B. Prasad, and S. Singh, *Sol. Energy*, **226**, 192 (2021).
6. P. M. Rajaitha, S. Hajra, K. Mistewicz, S. Panda, M. Sahu, D. Dubal, Y. Yamauchi, and H. J. Kim, *J. Mater. Chem. A Mater.*, **10**, 15906 (2022).
7. F. F. Abdi, L. Han, A. H. M. Smets, M. Zeman, B. Dam, and R. Van De Krol, *Nat. Commun.*, **4**, 2195 (2013).
8. Y. Liu, B. Zhang, D. Yan, and X. Xiang, *Green Chem.*, **26**, 2505 (2024).
9. D. Liu, J. C. Liu, W. Cai, J. Ma, H. B. Yang, H. Xiao, J. Li, Y. Xiong, Y. Huang, and B. Liu, *Nat. Commun.*, **10**, 2505–2524 (2019).
10. Y. Xue, Y. Wang, Z. Pan, and K. Sayama, *Angewandte Chemie - International Edition*, **60**, 10469 (2021).
11. E. Amaterz, A. Tara, A. Bouddouch, A. Taoufyq, B. Bakiz, A. Benlhachemi, and O. Jbara, *Rev. Environ. Sci. Biotechnol.*, **19**, 843 (2020).
12. X. M. C. Ta, R. Daiyan, T. K. A. Nguyen, R. Amal, T. Tran-Phu, and A. Tricoli, *Adv. Energy Mater.*, **12**, 2201358 (2022).
13. K. Obata, M. Schwarze, T. A. Thiel, X. Zhang, B. Radhakrishnan, I. Y. Ahmet, R. van de Krol, R. Schomäcker, and F. F. Abdi, *Nat. Commun.*, **14**, 6017 (2023).
14. M. Pourbaix, H. Zhang, and A. Pourbaix, *Mater. Sci. Forum*, **251–254**, 143 (1997).
15. Y. Zhang, W. Luc, G. S. Hutchings, and F. Jiao, *ACS Appl. Mater. Interfaces*, **8**, 24652 (2016).
16. X. Chang, T. Wang, P. Yang, G. Zhang, and J. Gong, *Adv. Mater.*, **31**, 1804710 (2019).

17. C. Kim, S. Choi, M. J. Choi, S. A. Lee, S. H. Ahn, S. Y. Kim, and H. W. Jang, *Appl. Sci.*, **10**, 3487 (2020).
18. W. Lu, Y. Zhang, J. Zhang, and P. Xu, *Ind. Eng. Chem. Res.*, **59**, 5536 (2020).
19. P. Ding, T. Jiang, N. Han, and Y. Li, *Mater. Today Nano*, **10**, 100077 (2020).
20. W. H. Cheng et al., *Adv. Energy Mater.*, **12**, 2201062 (2022).
21. B. Liu, T. Wang, S. Wang, G. Zhang, D. Zhong, T. Yuan, H. Dong, B. Wu, and J. Gong, *Nat. Commun.*, **13**, 7111 (2022).
22. L. K. Putri, B. J. Ng, W. J. Ong, S. P. Chai, and A. R. Mohamed, *Adv. Energy Mater.*, **12**, 2201093 (2022).
23. T. Abbas, H. S. M. Yahya, and N. A. S. Amin, *Energy Fuels*, **37**, 18330 (2023).
24. L. Wan, R. Chen, D. W. F. Cheung, L. Wu, and J. Luo, *J. Mater. Chem. A Mater.*, **11**, 12499 (2023).
25. S. Ashraf et al., "Exploring the frontiers of electrochemical CO_2 conversion: A comprehensive review." *Nano Materials Science* (2024).
26. D. Seo, A. Ma, T. Kwon, and K. M. Nam, *Inorg Chem. Front*, **11**, 998 (2024).
27. J. Kim, S. Jeong, M. Beak, J. Park, and K. Kwon, *Chem. Eng. J.*, **428**, 130259 (2022).
28. M. H. Lee et al., *Angewandte Chemie - International Edition*, **51**, 10760 (2012).
29. A. Paracchino, V. Laporte, K. Sivula, M. Grätzel, and E. Thimsen, *Nat. Mater.*, **10**, 456 (2011).
30. A. Paracchino, N. Mathews, T. Hisatomi, M. Stefik, S. D. Tilley, and M. Grätzel, *Energy Environ. Sci.*, **5**, 8673 (2012).
31. B. Seger, D. S. Tilley, T. Pedersen, P. C. K. Vesborg, O. Hansen, M. Grätzel, and I. Chorkendorff, *RSC Adv.*, **3**, 25902 (2013).
32. S. Cao, Z. Kang, Y. Yu, J. Du, L. German, J. Li, X. Yan, X. Wang, and Y. Zhang, *Adv. Energy Mater.*, **10**, 1902985 (2020).
33. F. Cui et al., *ACS Appl. Mater. Interfaces*, **13**, 30950 (2021).
34. A. Song, P. Bogdanoff, A. Esau, I. Y. Ahmet, I. Levine, T. Dittrich, T. Unold, R. van de Krol, and S. P. Berglund, *ACS Appl. Mater. Interfaces*, **12**, 13959 (2020).
35. G. K. Ramesha, J. F. Brennecke, and P. V. Kamat, *ACS Catal.*, **4**, 3249 (2014).
36. S. Ma, Y. Lan, G. M. J. Perez, S. Moniri, and P. J. A. Kenis, *ChemSusChem*, **7**, 866 (2014).
37. M. A. Farkhondehfal, S. Hernández, M. Rattalino, M. Makkee, A. Lamberti, A. Chiodoni, K. Bejtka, A. Sacco, F. C. Pirri, and N. Russo, *Int. J. Hydrogen Energy*, **45**, 26458 (2020).
38. W. Zhang, S. Zhu, Y. Li, and F. Wang, *Vacuum*, **82**, 328 (2007).
39. L.-Y. Qiao, F.-Y. Xie, M.-H. Xie, C.-H. Gong, W.-L. Wang, and J.-C. Gao, *Transactions of Nonferrous Metals Society of China (English Edition)*, **26**, 2109 (2016).
40. L. Couches, M. Interfaces, U. M. Constantine, C. De Développement, E. De, and M. Condensée, *Int. J. Nanoparticles*, **6**, 132 (2013).
41. M. Khosravi, M. R. Toroghinejad, M. R. Vaezi, and A. Saidi, *J. Mater. Sci., Mater. Electron.*, **31**, 7150 (2020).
42. Y. Furubayashi, T. Hitosugi, Y. Yamamoto, K. Inaba, G. Kinoda, Y. Hirose, T. Shimada, and T. Hasegawa, *Appl. Phys. Lett.*, **86**, 252101 (2005).
43. N. Yamada, T. Hitosugi, N. L. H. Hoang, Y. Furubayashi, Y. Hirose, T. Shimada, and T. Hasegawa, *Japanese Journal of Applied Physics, Part 1: Regular Papers and Short Notes and Review Papers*, **46**, 5275 (2007).
44. Y. Sato, H. Akizuki, T. Kamiyama, and Y. Shigesato, *Thin Solid Films*, **516**, 5758 (2008).
45. T. Hitosugi et al., *Appl. Phys. Express*, **1**, 111203 (2008).
46. Y. Sato, Y. Sanno, N. Oka, T. Kamiyama, and Y. Shigesato, *Materials Research Society Symposium Proceedings*, **1109**, 1 (2009).
47. C. Wang, J. Li, and J. Dho, *Materials Science and Engineering: B*, **182**, 1 (2014).
48. J. P. Niemelä, H. Yamauchi, and M. Karppinen, *Thin Solid Films*, **551**, 19 (2014).
49. Y. Liu, Q. Peng, Y. Qiao, and G. Yang, *J. Electron. Mater.*, **47**, 5334 (2018).
50. C. Jiang, Z. Wu, S. Xiao, Z. Ma, L. Liu, R. K. Y. Fu, P. K. Chu, H. Lin, and F. Pan, *Surf. Coat. Technol.*, **365**, 10 (2019).
51. W.-J. H. Berghuis, J. Melskens, B. Macco, S. B. Basuvalingam, M. A. Verheijen, and W. M. M. Kessels, *Journal of Vacuum Science & Technology A: Vacuum, Surfaces, and Films*, **38**, 022408 (2020).
52. B. R. Bricchi et al., *Mater Adv*, **2**, 7064 (2021).
53. Y. Lin et al., *J. Phys. Chem. C*, **119**, 2308 (2015).
54. O. Bienek, B. Fuchs, M. Kuhl, T. Rieth, J. Kühne, L. I. Wagner, L. M. Todenhagen, L. Wolz, A. Henning, and I. D. Sharp, *ACS Photonics*, **10**, 3985 (2023).
55. A. Jolivet et al., *Appl. Surf. Sci.*, **608**, 155214 (2023).
56. N. Inoue, H. Yuasa, and M. Okoshi, *Appl. Surf. Sci.*, **197–198**, 393 (2002).
57. Y. Hori, H. Wakebe, T. Tsukamoto, and O. Koga, *Electrochim. Acta*, **39**, 1833 (1994).
58. S. D. Kapusta and N. Hackerman, *Electrochim. Acta*, **25**, 1625 (1980).
59. N. Chen, C. Fang, X. Li, and W. Hu, *Electrochem. Commun.*, **127**, 107037 (2021).
60. C. F. Sanz-Navarro, S. F. Lee, S. S. Yap, C. H. Nee, and S. L. Yap, *Thin Solid Films*, **768**, 139697 (2023).
61. M. Drogowska, H. Ménard, and L. Brossard, *J. Appl. Electrochem.*, **21**, 84 (1991).
62. C. A. Gervasi, F. E. Varela, J. R. Vilche, and P. E. Alvarez, *Electrochim. Acta*, **42**, 537 (1997).
63. P. E. Alvarez, S. B. Ribotta, M. E. Folquer, C. A. Gervasi, and J. R. Vilche, *Corros. Sci.*, **44**, 49 (2002).
64. V. Brunetti and M. López Teijelo, *J. Electroanal. Chem.*, **613**, 9 (2008).
65. V. Brunetti and M. López Teijelo, *J. Electroanal. Chem.*, **613**, 16 (2008).
66. Y. Xie, X. Lu, W. Huang, and Z. Li, *Appl. Surf. Sci.*, **347**, 321 (2015).
67. S. Geiger, O. Kasian, A. M. Mingers, K. J. J. Mayrhofer, and S. Cherevko, *Sci. Rep.*, **7**, 4595 (2017).
68. H. Krýsová, M. Neumann-Spallart, H. Tarábková Paušová, P. Janda, J. Maixner, L. Kavan, and J. Krýsa, *Mater. Chem. Phys.*, **273**, 125038 (2021).
69. J. W. Schultze and M. M. Lohrengel, *Electrochim. Acta*, **45**, 2499 (2000).
70. R. O. Ansell, T. Dickinson, A. F. Povey, and P. M. A. Sherwood, *J. Electrochem. Soc.*, **124**, 1360 (1977).
71. X. Sun, M. Xie, J. J. Travis, G. Wang, H. Sun, J. Lian, and S. M. George, *J. Phys. Chem. C*, **117**, 22497 (2013).
72. H. Wang, G. Jia, Y. Guo, Y. Zhang, H. Geng, J. Xu, W. Mai, Q. Yan, and H. J. Fan, *Adv. Mater. Interfaces*, **3**, 1600375 (2016).
73. V. Sallaz, S. Poulet, J. Rouchou, J. M. Boissel, I. Chevalier, F. Voiron, Y. Lamy, and S. Oukassi, *ACS Appl. Energy Mater.*, **6**, 201 (2023).
74. R. Foudil and A. Djamila, *Portugaliae Electrochimica Acta*, **38**, 331 (2020).
75. B. Seger, T. Pedersen, A. B. Laursen, P. C. K. Vesborg, O. Hansen, and I. Chorkendorff, *J. Am. Chem. Soc.*, **135**, 1057 (2013).
76. A. S. Bakri, M. Z. Sahdan, F. Adriyanto, N. A. Raship, N. D. M. Said, S. A. Abdullah, and M. S. Rahim, *AIP Conf. Proc.*, **1788**, 030030 (2017).
77. S. Gürakar, H. Ot, S. Horzum, and T. Serin, *Materials Science and Engineering: B*, **262**, 114782 (2020).